{110}-Layered B-cation ordering in the anion-deficient perovskite $Pb_{2.4}Ba_{2.6}Fe_2Sc_2TiO_{13}$ with the crystallographic shear structure

{110}-layered B-cation ordering in the anion-deficient perovskite $Pb_{2.4}Ba_{2.6}Fe_2Sc_2TiO_{13}$ with the crystallographic shear structure

Oleg A. Tyablikov[a], Dmitry Batuk[b], Alexander A. Tsirlin[c], Maria Batuk[b], Valeriy Yu. Verchenko[a, c], Dmitry S. Filimonov[a], Konstantin V. Pokholok[a], Denis V. Sheptyakov[e], Marina G. Rozova[a], Joke Hadermann[b], Evgeny V. Antipov[a], Artem M. Abakumov[a, b]

[a] – *Department of Chemistry, Moscow State University, 119991, Leninskie Gory 1-3, Moscow, Russia*

[b] – *Electron Microscopy for Materials Science (EMAT), University of Antwerp, Groeneborgerlaan 171, B-2020, Antwerp, Belgium*

[c] – *National Institute of Chemical Physics and Biophysics, Akadeemia tee 23, 12618 Tallinn, Estonia*

[d] – *Laboratory for Neutron Scattering and Imaging, Paul Scherrer Institute, 5232 Villigen PSI, Switzerland*

Abstract

A novel anion-deficient perovskite-based compound, $Pb_{2.4}Ba_{2.6}Fe_2Sc_2TiO_{13}$, was synthesized via the citrate-based route. This compound is an $n = 5$ member of the $A_nB_nO_{3n-2}$ homologous series with unit-cell parameters related to the perovskite subcell $a_p \approx 4.0$ Å as $a_p\sqrt{2} \times a_p \times 5a_p\sqrt{2}$. The crystal structure of $Pb_{2.4}Ba_{2.6}Fe_2Sc_2TiO_{13}$ consists of quasi-2D perovskite blocks with a thickness of three octahedral layers sliced by the $\frac{1}{2}[110](\bar{1}01)_p$ crystallographic shear (CS) planes, which are parallel to the {110} plane of the perovskite subcell. The CS planes transform the corner-sharing octahedra into chains of edge-sharing distorted tetragonal pyramids. Using a combination of neutron powder diffraction, ^{57}Fe Mössbauer spectroscopy and atomic resolution electron energy-loss spectroscopy we demonstrate that the B-cations in $Pb_{2.4}Ba_{2.6}Fe_2Sc_2TiO_{13}$ are ordered along the {110} perovskite layers with Fe^{3+} in distorted tetragonal pyramids along the CS planes, Ti^{4+} preferentially in the central octahedra of the perovskite blocks and Sc^{3+} in the outer octahedra of the perovskite blocks. Magnetic susceptibility and Möessbauer spectroscopy indicate a broadened magnetic transition around

$T_N \sim 45$ K and the onset of local magnetic fields at low temperatures. The magnetic order is probably reminiscent of that in other $A_nB_nO_{3n-2}$ homologues, where G-type AFM order within the perovskite blocks has been observed.

Introduction

Because of its inherent flexibility, the ABO_3 perovskite structure can adopt a large variety of metal cations at both the A and B positions. Simultaneous population of these sites by more than one type of cation significantly expands the structural diversity of the perovskite family, particularly taking into account the structural phenomena related to the cation ordering. As the B-cations are responsible for the overwhelming majority of the functional properties of the perovskite-based materials, the importance of understanding and controlling their ordering patterns is well acknowledged and discussed in several reviews.[1–4] Some examples of intimate links between the B-site ordering in perovskites and their ferroelectric, magnetic and ion transport properties are provided by King and Woodward.[3] We can complement these examples with an extra illustration of this relationship, which at the same time demonstrates that achieving the desired ordering pattern of the B-cations is far from trivial. Double perovskite Bi_2FeCrO_6 with the Fe^{3+} and Cr^{3+} cations ordered along {111} planes was predicted from the first principles calculation to be a multiferroic combining the ferrimagnetic and ferroelectric properties.[5] The key issue is the B-cation ordering providing a path for ferromagnetic interactions between the e_g electrons of Fe^{3+} and the t_{2g} electrons of Cr^{3+}. This ordering is very difficult to achieve owing to close ionic radii and identical charge of Fe^{3+} and Cr^{3+}. Indeed, B-site disordered bulk Bi_2FeCrO_6 synthesized under high pressure conditions is paramagnetic at room temperature and shows a spin-glass transition below 130 K.[6] The B-site ordered Bi_2FeCrO_6 thin films were prepared with pulsed laser deposition (PLD) and the magnetization was demonstrated to correlate with the degree of the Fe/Cr ordering.[7] Therefore, the B-site ordering in perovskites can be the key to new functionalities, which justifies the importance of looking for new ordering patterns and pathways for their stabilization.

Although the number of possible combinations of the B-cations in the perovskite structure is huge, the number of possible ordering patterns is at the same time rather limited. In the majority of the B-site ordered perovskites, the B-cations of different types are arranged in alternating {111} layers.[2] The examples of the layered {001} ordering are scarce being confined to the small number of cuprates Ln_2CuMO_6 (Ln = La, Pr, Nd, Sm, Sr; M = Sn, Zr).[8–10] Specific requirements to the charge and size difference and the electronic structure are the main limiting

factors restricting the B-site ordering in perovskites. For example, the {001} layered ordering occurs in the compounds where one B-cation demonstrates a pronounced Jahn–Teller effect (e.g., Cu^{2+}) and there is a charge difference of 2 between the B and B' cations.[1] However, the situation changes drastically as the cation ordering is coupled with the ordering of oxygen vacancies in the anion-deficient perovskites.[11] In the $A_2BB'O_5$ brownmillerites, the {001} layered ordering of the B and B' cations is naturally stabilized by the alternation of the anion-complete (BO_2) layers and anion-deficient (B'O) layers, creating the octahedral and tetrahedral oxygen coordination for the B and B' cations, respectively.[12] Thus, the cation ordering is driven not only by the charge and size difference, but merely by the difference in coordination preferences of the cations.

To the best of our knowledge, no perovskite with the ordered arrangement of different B-cations along the {110} perovskite planes has been observed so far. Coupling cation and anion-vacancy ordering works effectively for the {001} perovskite planes, but there is no anion-vacancy ordering pattern confined to the {110} plane of the perovskite structure as the anion vacancies tend to segregate along the {001} planes, <100> or <110> cubic directions.[13] Crystallographic shear (CS) planes in perovskites provide an alternative template which can be used for generating the {110} B-site ordering employing a difference in the affinity of the B-cations to different coordination numbers. The $1/m$[umv]$(hkl)_p$ (subscript "p" denotes the perovskite structure) CS plane cuts a parent perovskite structure along a certain $(hkl)_p$ crystallographic plane and displaces one part of the structure relative to another using $1/m$[umv] displacement vector.[14–16] Periodical and equidistant occurrence of the $\frac{1}{2}[110](\bar{1}01)_p$ CS planes (parallel to the {110} plane of the perovskite subcell) leads to formation of the oxygen-deficient homologous series $A_nB_nO_{3n-2}$.[17] The structure of the $A_nB_nO_{3n-2}$ compounds is built of perovskite blocks with $(n-2)$ BO_6 octahedral layers, which are stacked along the [101] crystallographic direction of the initial perovskite structure and connected to each other by quasi-2D $A_2B_2O_4$ blocks. These blocks are built of chains of edge-shared BO_5 distorted tetragonal pyramids. Thus the CS operation creates the {110}-layered arrangement of the coordination polyhedra with distinct coordination numbers (5 and 6) and can be used to promote the corresponding B-site ordering.

In this paper, we employ this method to design a {110}-layered B-site ordered perovskite and report on the synthesis and crystal structure of the new n = 5 member of $A_nB_nO_{3n-2}$ homologous series $Pb_{2.4}Ba_{2.6}Fe_2Sc_2TiO_{13}$. Using a combination of neutron powder diffraction, [57]Fe Mössbauer spectroscopy and atomic resolution electron energy-loss spectroscopy we demonstrate that the B-cations are ordered along the {110} perovskite layers with Fe^{3+} in

distorted tetragonal pyramids along the CS planes, Ti^{4+} in the central octahedra of the perovskite blocks and Sc^{3+} in the outer octahedra of the perovskite blocks.

Experimental section

The samples were prepared via citrate-based route. First, water solution of Pb^{2+}, Ba^{2+}, Fe^{3+}, Sc^{3+} nitrates was prepared according to the Pb:Ba:Fe:Sc = 3:2:2:2 molar ratio. The stoichiometric amounts of $Pb(NO_3)_2$ (99.99%), $Ba(NO_3)_2$ (prepared by dissolving $BaCO_3$ (99.99%) in nitric acid), $Sc(NO_3)_3*4H_2O$ (99.99%) and $Fe(NO_3)_3*9H_2O$ were added to a melt of citric acid monohydrate (99.99%). To this melt a water solution of ammonium citratoperoxotitanate, prepared from TiO_2 (99.99%)[18], was added. The resulting solution was evaporated to yield a viscous mixture, which was then annealed at 850°C in air for 12 hours producing a black powder. The powder was pressed into pellets and annealed at 950-970°C for 50 hours with two intermediate regrindings.

The phase composition of the samples and the unit cell parameters were determined using powder X-ray diffraction (PXRD) data obtained with a Huber Guinier powder diffractometer ($Cu_{K\alpha 1}$ (1.54056 Å), curved Ge (111) monochromator, transmission mode, image plate).

The cation composition was measured by energy-dispersive X-ray (EDX) analysis using a JEOL 5510 scanning electron microscope (SEM) equipped with an INCAx-sight 6587 system (Oxford instruments). The EDX spectra from 40 crystallites were collected, and the Pb-M, Ba-L, Fe-K, Sc-K, and Ti-K lines were used to determine the elemental composition.

Mössbauer spectroscopy (^{57}Fe) was performed on the samples enriched with ^{57}Fe (20%) in a transmission mode using a constant acceleration Mössbauer spectrometer (MS1104, Rostov-na-Donu, Russia) with ^{57}Co/Rh γ-ray sources. Velocities were calibrated with the standard α-Fe or sodium nitroprusside absorbers, isomer shifts were related to α-Fe. Spectra treatment was performed using ''UnivemMS''[19] and custom software.

Neutron powder diffraction (NPD) data were collected with the high resolution powder diffractometer HRPT at the Swiss spallation neutron source (SINQ, Paul Scherrer Institute (PSI), Villigen, Switzerland). The data were collected at 300 K with the wavelength $\lambda = 1.4940$ Å and at 2 K with the wavelength $\lambda = 1.8856$ Å using a standard orange cryostat. The Rietveld refinement of the crystal structure against the NPD data was performed with the JANA2006 package.[20]

Samples for the TEM study were prepared by grinding the material under ethanol and depositing a few drops of the suspension onto copper grids covered by a holey carbon layer.

Electron diffraction (ED) patterns were obtained with a Philips CM20 transmission electron microscope (TEM) operated at 200 kV. High-angle annular dark-field scanning transmission electron microscopy (HAADF-STEM) images and STEM electron energy-loss spectroscopy (STEM-EELS) elemental maps were obtained with a probe aberration-corrected FEI Titan 80-300 "cubed" microscope operated at 120 kV. The data were recorded using a probe with a convergence semi-angle 21 mrad (with a probe size of about 1 Å) and the probe current about 45 pA. Acquisition was done in the spectrum imaging mode (SI), so that the electron probe was scanned over the sample and in each point an EELS spectrum was acquired together with a HAADF signal as an image reference. The individual elemental distribution maps were generated by placing an integration window over the background-subtracted absorption edges of the elements ($Sc-L_{2,3}$; $Ti-L_{2,3}$; $Fe-L_{2,3}$).

Magnetization was measured using the vibrating sample magnetometer (VSM) setup of Quantum Design PPMS in the temperature range $5-380$ K in applied fields up to 5 T. Heat capacity was measured by relaxation method using Quantum Design PPMS in the temperature range $1.8-60$ K in zero magnetic field.

Results

The room-temperature PXRD pattern revealed the appearance typical for the members of the $A_nB_nO_{3n-2}$ homologous series (Fig. 1). The pattern can be indexed in the orthorhombic crystal system with an A-centered unit cell with the parameters $a = 5.8252(1)$ Å, $b = 4.0647(1)$ Å, $c = 27.1226(5)$ Å. The room temperature electron diffraction patterns taken along the main crystallographic directions (Fig. 2) agree with the unit cell parameters and the lattice centering derived from the PXRD data. According to the PXRD data, the sample contains a small amount of the Sc_2O_3 admixture (the maximum intensity is ~5%). EDX analysis demonstrates the cation composition $Pb_{2.3(2)}Ba_{2.7(2)}Fe_{2.0(1)}Sc_{2.2(2)}Ti_{0.8(1)}$ that agrees with the initial composition of the sample for the transition metal atomic ratio, but shows smaller Pb/Ba ratio. This discrepancy can be attributed to possible loss of Pb during the synthesis because of the relatively high volatility of lead oxide. It should be noted that the cation composition determined with the EDX analysis is in a good agreement with that obtained in the course of the Rietveld refinement providing the $Pb_{2.4}Ba_{2.6}Fe_2Sc_2TiO_{13}$ formula (see below).

The crystal structure refinement of $Pb_{2.4}Ba_{2.6}Fe_2Sc_2TiO_{13}$ was performed from room temperature (RT, T = 300 K) and low temperature (LT, T = 2 K) NPD data. The structural parameters of $Pb_2Ba_2BiFe_5O_{13}$[21] were used as a starting model. It is known that the n = 5

$A_nB_nO_{3n-2}$ members can exist as two *Ammm* and *A2/m* polymorphs. Both possibilities were tested in the refinement of the RT structure. In the *A2/m* model, the refined monoclinic β-angle was very close to 90° $(90.055(9)^o)$ and the reliability factors for the monoclinic model were slightly higher compared to those of the orthorhombic structure ($R_F = 0.018$, $R_P = 0.026$ (*A2/m*) and $R_F = 0.016$, $R_P = 0.026$ (*Ammm*)). Thus, the orthorhombic model was selected for the final refinement. For the LT pattern, contrarily, the refined monoclinic angle noticeably deviates from 90° $(90.257(3)^o)$ pointing to the *A2/m* model. This indicated that the RT and LT phases are related by a second order phase transition, as it was previously observed for other $A_nB_nO_{3n-2}$ compounds.[21,22]

The coordination environment of the A positions in the six-sided tunnels at the CS planes (the A1 position, see Table 3) is suitable only for cations with a lone electron pair, and is occupied by Pb^{2+} in all perovskites with the CS structure. This position was populated by Pb only. The A2 and A3 positions in the perovskite blocks were jointly populated by Pb and Ba and their ratio was refined. The starting population of the B positions was inferred from the atomic resolution compositional STEM-EELS mapping (Fig. 3). The atomic resolution STEM-EELS maps of Fe, Sc, Ti demonstrate that the Fe cations are concentrated in the edge-sharing distorted tetragonal pyramids at the CS planes (the B1 position), with some minor fraction in the outer octahedral layers of the perovskite block and even smaller population of the inner octahedral layer (see intensity profiles in Fig. S1 and S2 of Supporting Information). The Sc cations are distributed over the inner and outer octahedral layers (the B2 and B3 positions, respectively), whereas the Ti cations are mostly concentrated in the inner layer. Thus, STEM-EELS provides direct and unequivocal proof of the {110}-layered B-site ordering.

The LT refinement of the atomic displacement parameter (ADP) for the B1 position populated by the Fe cations only resulted in relatively high ADP of $0.0145(9)Å^2$, and renders the ADP for the B2 position strongly negative. Decreasing the occupancy factor of the B1 position brings the ADPs back to physically reasonable values. Careful inspection of the STEM-EELS maps revealed that a small fraction of the Ti cations can also be located at the B1 position. Taking into account the strongly different scattering lengths for the Fe and Ti cations (9.450 fm and -3.438 fm, respectively), it is not surprising that the minor fraction of Ti can substantially change the overall scattering power. The occupancy factor for the B1 position was determined as 0.92Fe+0.08Ti. The scattering power of the B2 and B3 positions was refined by populating them with the Sc cations (12.290 fm) and refining the occupancy factors. As three species with different scattering lengths (Sc, Ti and Fe) should be simultaneously present in these positions, their distribution cannot be refined directly. The fractions of these cations in the B2 and B3

positions were settled according to the refined total scattering power, the determined chemical composition of the compound and qualitative cation distribution observed with STEM-EELS. The occupancy factors provided in Table 3 allowed us to perform satisfactory refinements at both LT and RT and obtain good reliability factors. As the Mössbauer spectra (see below) indicate the single oxidation state +3 for the Fe cations, the occupancies of the oxygen positions were not refined. Similar to $Pb_2Ba_2BiFe_5O_{13}$[21], in the RT *Ammm* structure the O4 atom was displaced along the *a* axis from the 4-fold position to the 8-fold position with halved occupancy to avoid extremely large ADP. The final refinement was carried out in an isotropic approximation for all ADPs for both experiments. Second phase (Sc_2O_3, ~ 3.5 wt.%) was also added to the refinements. Experimental, calculated and different NPD profiles for the RT and LT data are shown in Fig. 4. Crystallographic parameters, atomic coordinates and main interatomic distances are listed in Tables 1 - 5. The crystal structure was visualized using HAADF-STEM imaging. Fig. 5 represents the HAADF-STEM image of $Pb_{2.4}Ba_{2.6}Fe_2Sc_2TiO_{13}$ taken along the [010] direction. The double columns of the Pb atoms in the six-sided tunnels and A-positions of the perovskite blocks appear very bright ($Z_{Pb} = 82$, $Z_{Ba} = 56$), while the B-positions of the perovskite blocks are seen as equally weak spots owing to close atomic numbers of Sc, Ti and Fe ($Z_{Fe} = 26$, $Z_{Sc} = 21$, $Z_{Ti} = 22$).

Mössbauer spectra of $Pb_{2.4}Ba_{2.6}Fe_2Sc_2TiO_{13}$ were measured in the temperature range from RT down to 4.2 K. At RT, the spectrum comprises several heavily overlapped paramagnetic doublets (Fig. 6). According to their isomer shifts (ISs) (Table S1 of Supporting information), they all belong to oxygen-coordinated Fe^{3+} cations.[23] At 0.31 and 0.34 mm/s, the ISs of the two major doublets (D1, 2) are very similar, and, thus, the corresponding Fe^{3+} cations are in the identical coordination. The average value of their quadrupole shifts ($<\Delta E_Q> = 0.72$ mm/s) are akin to the analogous values of Fe^{3+} cations in five-fold pyramidal coordination in the other members of the $A_nB_nO_{3n-2}$ homologous series.[17,21,22,24] The difference in ΔE_Qs of these doublets is attributed to local distortions caused by altering neighboring Sc^{3+} or Ti^{4+} cations. Accordingly, their spectral contribution ratio, close to ~2:1, correlates semi-quantitatively (because of strong overlapping) with the Sc and Ti content. The third minor (~7%) doublet (D3 in Table S1) is to be assigned to Fe^{3+} in octahedral coordination. At T = 78 K, the spectrum is still paramagnetic, but the line widths of constituting doublets slightly increases as well as their overlap (Fig. 6). As a result, the spectrum is fit well using a single doublet (Table S1 of Supporting information). At T = 4.2 K the Mössbauer spectrum is magnetically split (Fig. 6). Its spectrum consists of superposition of several broadened Zeeman sextet components. The minor sextet, shown as a dashed line in Fig. 6, corresponds to Fe^{3+} cations in octahedral coordination according to its hyperfine parameters. Its relative spectral area scales to 9% that agrees well with 8% of Fe^{3+} in

the octahedral B2 and B3 positions as refined from the NPD data. The major component, assigned to Fe^{3+} cations in the tetragonal pyramidal B1 position, is significantly broadened. For that reason, it is fitted using hyperfine magnetic field distribution (HFD) (Fig. 6) with an average value of the magnetic hyperfine field (H_{hf}) of <44.9 T>, obtained by Hesse–Rubartsch method [25] (Table S1 of Supporting information). The relatively low <H_{hf}> value, compared to other members of the $A_nB_nO_{3n-2}$ homologous series with the higher occupancy of octahedral sites by Fe^{3+} cations in the perovskite block, follows the common trend of decreasing H_{hf} with increasing content of the diamagnetic cations in the perovskite block.

The magnetic susceptibility of $Pb_{2.4}Ba_{2.6}Fe_2Sc_2TiO_{13}$ (Fig. 7) gradually increases toward low temperatures. Above 250 K, it follows the Curie-Weiss law $\chi = C/(T-\theta)$ with the Curie constant $C = 6.84$ emu K/mol and the Curie-Weiss temperature $\theta = -289$ K (Fig. 7, inset). The C value yields the paramagnetic effective moment $\mu_{eff} = 5.23$ μ_B/Fe that is slightly below the spin-only value of 5.92 μ_B for Fe^{3+}. This discrepancy may be due to the limited temperature range of the fitting. The negative value of θ indicates predominant antiferromagnetic interactions between the Fe^{3+} ions. For a spin chain built of $S = 5/2$ ions, $\theta = -S(S+1)/3*2J_{eff}$, so that an effective intrachain coupling is $J_{eff} \sim 50$ K. In $Pb_{2.4}Ba_{2.6}Fe_2Sc_2TiO_{13}$, J_{eff} is a combination of the nearest-neighbor (J_1) and next-nearest-neighbor (J_2) interactions along the chain. Our estimate of $J_{eff} \sim 50$ K can be compared to $J_{eff} = J_1 + J_2 \sim 82$ K for the n = 4 $PbBaFe_2O_5$ CS structure, where we used *ab initio* values of $J_1 \sim$ -8 K and $J_2 \sim 90$ K.[22]

Around 45 K, a weak bend in the magnetic susceptibility of $Pb_{2.4}Ba_{2.6}Fe_2Sc_2TiO_{13}$ is observed. Additionally, field dependence of $\chi(T)$ is clearly visible below 80 K. However, neither below nor above 45 K any appreciable ferromagnetic signal could be detected. Field dependence of the magnetization measured at 5 K (not shown) confirms that the $Pb_{2.4}Ba_{2.6}Fe_2Sc_2TiO_{13}$ sample lacks any remnant magnetization. Therefore, the weak field dependence of $\chi(T)$ is likely extrinsic.

When considered on its own, the bend around 45 K can hardly be interpreted as a regular magnetic transition. Smooth and featureless heat capacity of $Pb_{2.4}Ba_{2.6}Fe_2Sc_2TiO_{13}$ in this temperature range (Fig. 7, inset) is not supportive of the magnetic transition either. On the other hand, the Mössbauer spectra give clear evidence for the magnetic order that is present at low temperatures. Therefore, $Pb_{2.4}Ba_{2.6}Fe_2Sc_2TiO_{13}$ exhibits antiferromagnetic order at low temperatures, but this order is local in nature. The difference pattern obtained by subtracting the RT NPD data from the LT data shows weak diffuse intensity near $2\theta = 23.1^o$ (Fig. S3 of Supporting Information), which corresponds to the position of the most intense magnetic

1,1/2,1/2 reflection of the AFM-ordered isostructural $Pb_2Ba_2BiFe_5O_{13}$.[21] This diffuse intensity indicates at least local correlations between the spins at low temperatures. The weakness of the magnetic diffuse scattering and insufficient signal-to-noise ratio does not allow quantitative fitting of the diffuse intensity profile. However, it is obvious that the angular distribution of the diffuse intensity is rather symmetric that differs significantly from the strongly asymmetric shape of the Warren-type diffuse scattering typical for the magnetic short-range order in two dimensions.[26] This suggests that the magnetic order in $Pb_{2.4}Ba_{2.6}Fe_2Sc_2TiO_{13}$ is 3D, but broken into small domains that broaden magnetic reflections dramatically.

Discussion

The RT and LT crystal structures of $Pb_{2.4}Ba_{2.6}Fe_2Sc_2TiO_{13}$ are shown in Fig.8a,b. The crystal structure of $Pb_{2.4}Ba_{2.6}Fe_2Sc_2TiO_{13}$ consists of alternating blocks with the 6-fold and 5-fold coordinated B-cations. Corner-sharing BO_6 octahedra form quasi-2D perovskite blocks, which are interleaved by blocks of distorted tetragonal BO_5 pyramids. These pyramids are connected by edge-sharing into chains running along the b-axis. The chains can adopt two mirror-related configurations, which can be arbitrarily called "left" (L) and "right" (R) (Fig.8c), depending on the direction of the displacement of the O4 atom along the a-axis away from the m_x mirror plane. In case of the orthorhombic structure with $Ammm$ space group the L and R chains are randomly distributed leading to the splitting of the O4 position. Lowering the temperature freezes the configuration of the chains, removes the m_x mirror plane and decreases the symmetry down to $A2/m$, where the CS planes with either L or R chains are ordered in alternating fashion.

The most remarkable feature of the $Pb_{2.4}Ba_{2.6}Fe_2Sc_2TiO_{13}$ structure is the pronounced {110}-layered ordering of the Fe^{3+}, Sc^{3+} and Ti^{4+} cations. The vast majority (92%) of the Fe^{3+} cations is concentrated in the BO_5 tetragonal pyramids at the CS planes. This can be attributed to the d^5 high spin electron configuration of Fe^{3+}, which implies absence of a crystal field stabilization and hence no energetic preference of the octahedral coordination over tetragonal pyramidal coordination. The 5-fold oxygen coordination provides an optimal bond valence balance for the Fe^{3+} cations (BVS = 3.0 for the Fe atoms at the B1 position with the parameters of the RT structure). Size difference apparently also plays a role. The B1 cations form two B1-O3 bonds of 1.878 Å, that is too short for the relatively large Sc^{3+} cations (r = 0.745 Å, CN = 6), which, moreover, have a strong affinity towards the octahedral coordination. Smaller Ti^{4+} (r = 0.51 Å, CN = 5) can occur in tetragonal pyramidal coordination[27–33] and a minor fraction of the Ti cations was indeed observed at the B1 position. The Ti^{4+} cations prefer the B3 octahedral

position at the center of the perovskite block, that can be related to the requirement of obeying local electroneutrality, as the A positions around this inner octahedral layer are occupied by divalent Pb and Ba cations. By comparing the different $A_nB_nO_{3n-2}$ structures it was established that the charge difference is the main driving force for the uneven cation distribution within the perovskite block.[24]

The n = 4, 5, 6 $A_nB_nO_{3n-2}$ (B = Fe) ferrites demonstrate robust antiferromagnetism with the relatively high Néel temperature of ~ 625-630 K, which is practically independent of the homologue number.[21,22] Diluting the Fe cations with non-magnetic Ti^{4+}, Sc^{3+} or Sn^{4+} cations substantially decreases T_N, but does not alter the long-range AFM spin arrangement.[17,24,34] In $Pb_{2.4}Ba_{2.6}Fe_2Sc_2TiO_{13}$ the {110}-layered B-site ordering results in almost complete substitution of the Fe^{3+} cations in the perovskite blocks with Sc^{3+} and Ti^{4+}, suppressing the regular long-range AFM ordering. Local order is established instead below $T_N \approx 45$ K. This local order is probably reminiscent of that in other $A_nB_nO_{3n-2}$ homologues and becomes frequently interrupted owing to various interaction pathways between the magnetic layers through the minority Fe atoms in the perovskite blocks that results in the small size of the ordered magnetic domains.

Conclusions

We have prepared a new n = 5 member of the $A_nB_nO_{3n-2}$ homologous series $Pb_{2.4}Ba_{2.6}Fe_2Sc_2TiO_{13}$. Its crystal structure consists of perovskite blocks alternating with anion-deficient blocks with the CS structure. The $\frac{1}{2}[110](\bar{1}01)_p$ CS planes in $Pb_{2.4}Ba_{2.6}Fe_2Sc_2TiO_{13}$ are parallel to the {110} plane of the perovskite subcell and thus provide a template for generating the {110} B-site ordering for the cations that tend towards the different coordination environment. In $Pb_{2.4}Ba_{2.6}Fe_2Sc_2TiO_{13}$, the Fe^{3+} cations are almost fully occupy positions in the distorted tetragonal pyramids at the CS planes; Ti^{4+} are preferentially located at the most symmetrical central octahedra of the perovskite blocks and Sc^{3+} prefer the slightly distorted outer octahedra of the perovskite blocks. In spite of the significant spatial separation of the Fe cation, $Pb_{2.4}Ba_{2.6}Fe_2Sc_2TiO_{13}$ demonstrates 3D short-range antiferromagnetic correlations below $T_N \approx 45$ K, as determined from the magnetic susceptibility measurements. According to the neutron powder diffraction data measured at 2 K, the local spin order in $Pb_{2.4}Ba_{2.6}Fe_2Sc_2TiO_{13}$ seems to be reminiscent to that of other $A_nB_nO_{3n-2}$ homologues.

Acknowledgements

References

1.   M. Anderson, K. Greenwood, G. Taylor, and K. R. Poeppelmeier, *Prog. Solid State Chem.*, 1993, **22**, 197–233.

2.   P. K. Davies, H. Wu, A. Y. Borisevich, I. E. Molodetsky, and L. Farber, *Annu. Rev. Mater. Res.*, 2008, **38**, 369–401.

3.   G. King and P. M. Woodward, *J. Mater. Chem.*, 2010, **20**, 5785–5796.

4.   A. M. Abakumov, A. A. Tsirlin, and E. V. Antipov, in *Comprehensive Inorganic Chemistry II, Volume 2: Transition Elements, Lanthanides and Actinides*, eds. J. Reedijk and K. Poeppelmeier, Elsevier Ltd., Second Edi., 2013, pp. 1–40.

5.   P. Baettig, C. Ederer, and N. Spaldin, *Phys. Rev. B*, 2005, **72**, 214105.

6.   M. R. Suchomel, C. I. Thomas, M. Allix, M. J. Rosseinsky, A. M. Fogg, and M. F. Thomas, *Appl. Phys. Lett.*, 2007, **90**, 112909.

7.   R. Nechache, C. Harnagea, L.-P. Carignan, O. Gautreau, L. Pintilie, M. P. Singh, D. Ménard, P. Fournier, M. Alexe, and A. Pignolet, *J. Appl. Phys.*, 2009, **105**, 061621.

8.   M. T. Anderson and K. R. Poeppelmeier, *Chem. Mater.*, 1991, **3**, 476–482.

9.   M. T. Anderson, K. R. Poeppelmeier, S. A. Gramsch, and J. K. Burdett, *J. Solid State Chem.*, 1993, **102**, 164–174.

10.   M. Azuma, S. Kaimori, and M. Takano, *Chem. Mater.*, 1998, **10**, 3124–3130.

11.   E. V Antipov, A. M. Abakumov, and S. Y. Istomin, *Inorg. Chem.*, 2008, **47**, 8543–8552.

12.   A. M. Abakumov, M. G. Rozova, and E. V Antipov, *Russ. Chem. Rev.*, 2004, **73**, 847–860.

13.   M. T. Anderson, J. T. Vaughey, and K. R. Poeppelmeier, *Chem. Mater.*, 1993, **5**, 151–165.

14.   A. M. Abakumov, J. Hadermann, S. Bals, I. V. Nikolaev, E. V. Antipov, and G. Van Tendeloo, *Angew. Chem. Int. Ed. Engl.*, 2006, **45**, 6697–6700.

15. A. M. Abakumov, J. Hadermann, G. Van Tendeloo, and E. V. Antipov, *J. Am. Ceram. Soc.*, 2008, **91**, 1807–1813.

16. A. M. Abakumov, D. Batuk, J. Hadermann, M. G. Rozova, D. V. Sheptyakov, A. A. Tsirlin, D. Niermann, F. Waschkowski, J. Hemberger, G. Van Tendeloo, and E. V. Antipov, *Chem. Mater.*, 2011, **23**, 255–265.

17. A. M. Abakumov, J. Hadermann, M. Batuk, H. D'Hondt, O. A. Tyablikov, M. G. Rozova, K. V. Pokholok, D. S. Filimonov, D. V. Sheptyakov, A. A. Tsirlin, D. Niermann, J. Hemberger, G. Van Tendeloo, and E. V. Antipov, *Inorg. Chem.*, 2010, **49**, 9508–9516.

18. M. Tada, K. Tomita, V. Petrykin, and M. Kakihana, *Solid State Ionics*, 2002, **151**, 293–297.

19. V. Petříček, M. Dušek, and L. Palatinus, *Zeitschrift für Krist. - Cryst. Mater.*, 2014, **229**, 345–352.

20. S. A. Bruggemann, Y. A. Artzybashev, and S. V. Orlov, 1993, UNIVEM, Version 4.5.

21. A. M. Abakumov, M. Batuk, A. A. Tsirlin, O. A. Tyablikov, D. V. Sheptyakov, D. S. Filimonov, K. V. Pokholok, V. S. Zhidal, M. G. Rozova, E. V. Antipov, J. Hadermann, and G. Van Tendeloo, *Inorg. Chem.*, 2013, **52**, 7834–7843.

22. I. V. Nikolaev, H. D'Hondt, A. M. Abakumov, J. Hadermann, A. M. Balagurov, I. A. Bobrikov, D. V. Sheptyakov, V. Y. Pomjakushin, K. V. Pokholok, D. S. Filimonov, G. Van Tendeloo, and E. V. Antipov, *Phys. Rev. B*, 2008, **78**, 024426.

23. F. Menil, *J. Phys. Chem. Solids*, 1985, **46**, 763–789.

24. M. Batuk, O. A. Tyablikov, A. A. Tsirlin, S. M. Kazakov, M. G. Rozova, K. V. Pokholok, D. S. Filimonov, E. V. Antipov, A. M. Abakumov, and J. Hadermann, *Mater. Res. Bull.*, 2013, **48**, 3459–3465.

25. J. Hesse and A. Rubartsch, *J. Phys. E.*, 1974, **7**, 526–532.

26. B. Warren, *Phys. Rev.*, 1941, **59**, 693–698.

27. M. Batuk, D. Batuk, A. M. Abakumov, and J. Hadermann, *J. Solid State Chem.*, 2014, **215**, 245–252.

28. P. B. Moore and J. Louisnathan, *Science*, 1967, **156**, 1361–1362.

29. T. Höche, C. Rüssel, and W. Neumann, *Solid State Commun.*, 1999, **110**, 651–656.

30. M. A. Roberts, G. Sankar, J. M. Thomas, R. H. Jones, H. Du, J. Chen, W. Pang, and R. Xu, *Nature*, 1996, **381**, 401–404.

31. R. Werthmann and R. Hoppe, *Zeitschrift för Anorg. und Allg. Chemie*, 1985, **523**, 54–62.

32. C. Weiss and R. Hoppe, *Zeitschrift för Anorg. und Allg. Chemie*, 1995, **621**, 1447–1453.

33.   R. D. Aughterson, G. R. Lumpkin, M. D. L. Reyes, N. Sharma, C. D. Ling, B. Gault, K. L. Smith, M. Avdeev, and J. M. Cairney, *J. Solid State Chem.*, 2014, **213**, 182–192.

34.   O. E. Korneychik, M. Batuk, A. M. Abakumov, J. Hadermann, M. G. Rozova, D. V. Sheptyakov, K. V. Pokholok, D. S. Filimonov, and E. V. Antipov, *J. Solid State Chem.*, 2011, **184**, 3150–3157.
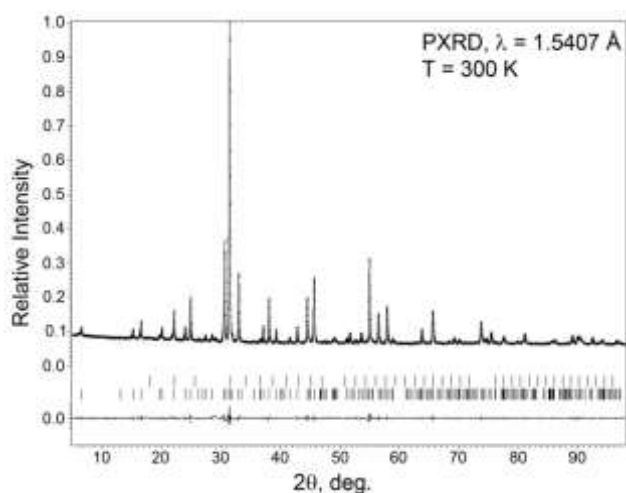
Figures

Figure 1. Experimental, calculated and difference PXRD profiles for $Pb_{2.4}Ba_{2.6}Fe_2Sc_2TiO_{13}$ after the Le Bail fitting. The bottom row of reflections corresponds to the $Pb_{2.4}Ba_{2.6}Fe_2Sc_2TiO_{13}$ phase, the top row – to the Sc_2O_3 phase.
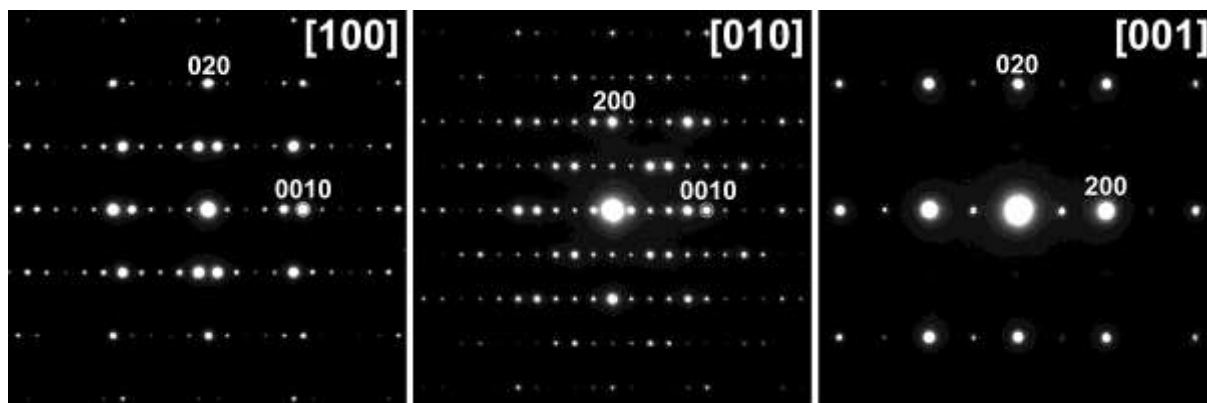
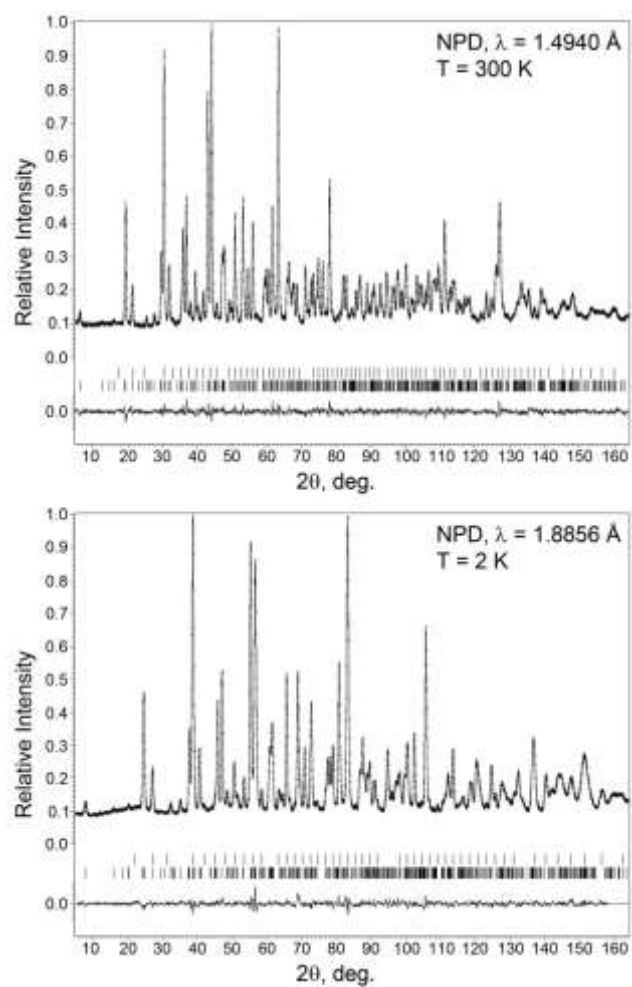Figure 2. Electron diffraction patterns taken along the [100], [010] and [001] directions.

Figure 3. Experimental, calculated and difference NPD profiles for $Pb_{2.4}Ba_{2.6}Fe_2Sc_2TiO_{13}$ after the Rietveld refinement at 300 K and 2 K. On both patterns, the bottom row of reflections corresponds to the $Pb_{2.4}Ba_{2.6}Fe_2Sc_2TiO_{13}$ phase, the top row – to the Sc_2O_3 phase.
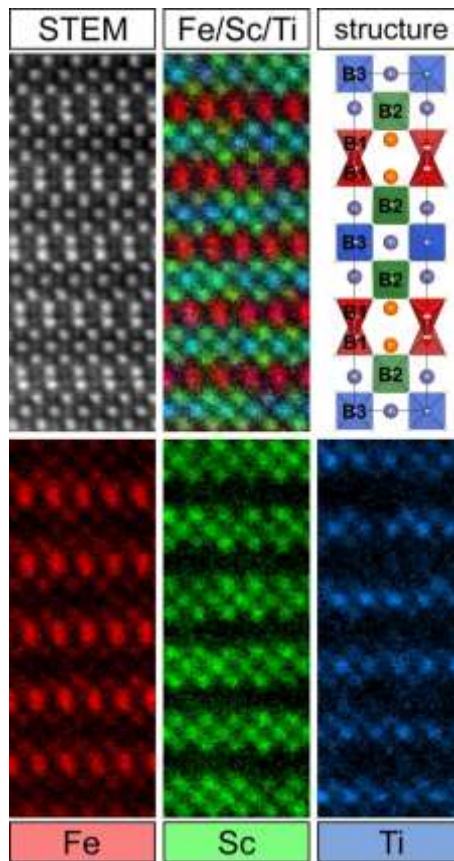
Figure 4. (Top row, left to right) [010] High resolution HAADF-STEM image of $Pb_{2.4}Ba_{2.6}Fe_2Sc_2TiO_{13}$; elemental distribution map obtained using STEM-EELS technique and the unit cell of the refined structure with the indicated B-site atomic positions. (Bottom row) Individual STEM-EELS elemental maps for Fe, Sc and Ti.
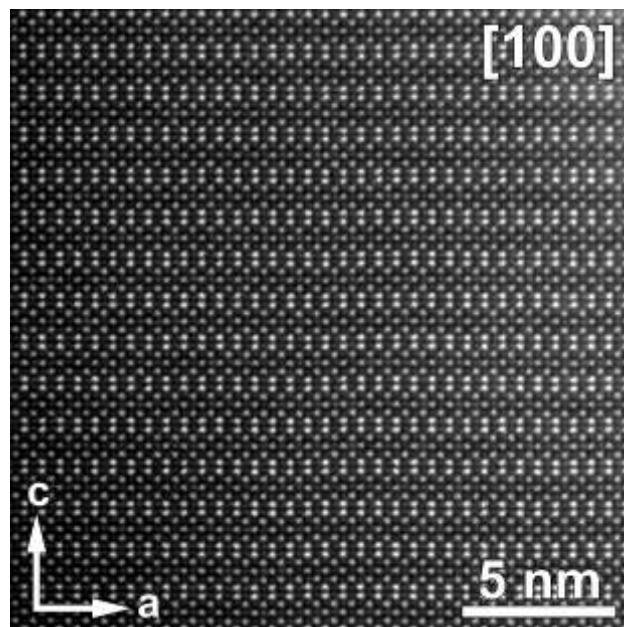

Figure 5. HAADF-STEM image of $Pb_{2.4}Ba_{2.6}Fe_2Sc_2TiO_{13}$ taken along the [010] direction.

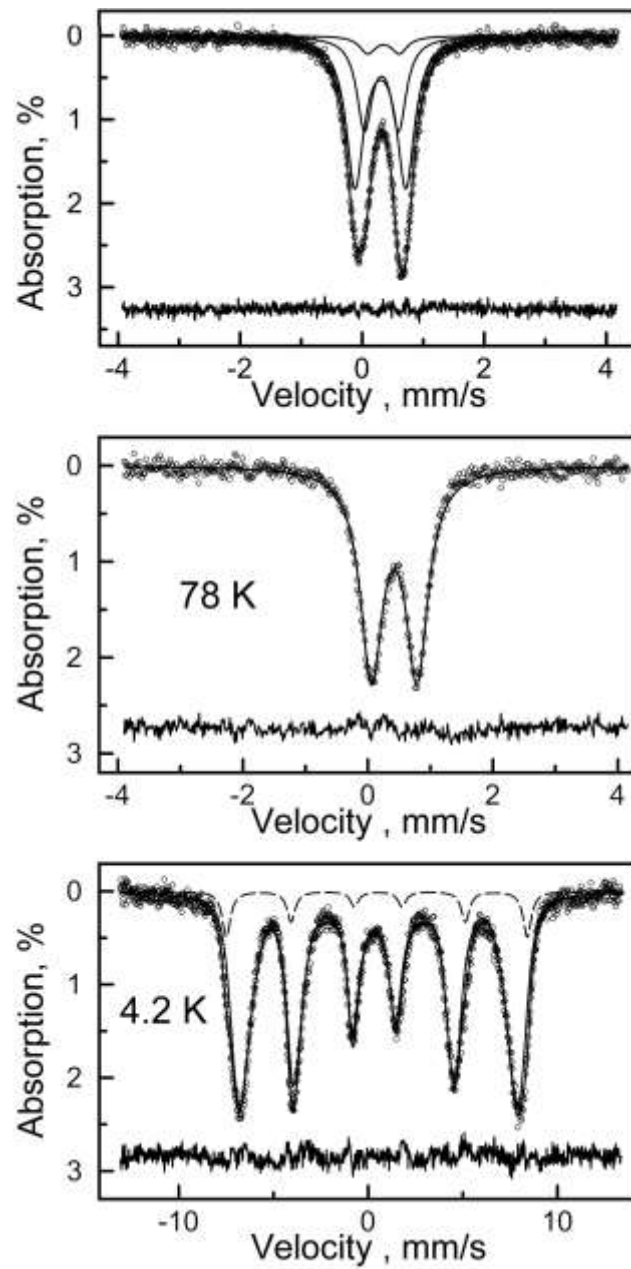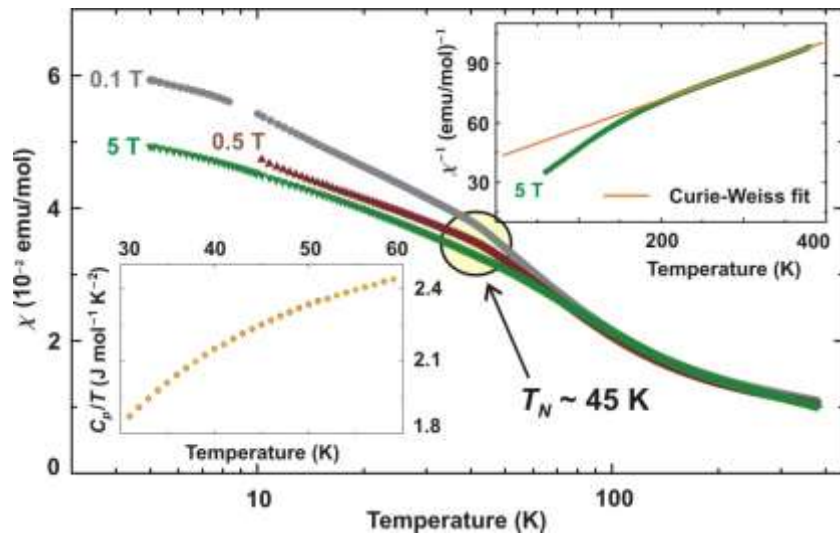Figure 6. ^{57}Fe Mossbauer spectra of $Pb_{2.4}Ba_{2.6}Fe_2Sc_2TiO_{13}$ taken at indicated temperatures.

Figure 7. Magnetic susceptibility of $Pb_{2.4}Ba_{2.6}Fe_2Sc_2TiO_{13}$ measured in applied fields of 0.1, 0.5 and 5 T. The arrow shows the Néel temperature $T_N \approx 45$ K. The insets show heat capacity dependence in $30 - 60$ K temperature range (left inset) and Curie-Weiss fitting of 5 T curve (right inset).
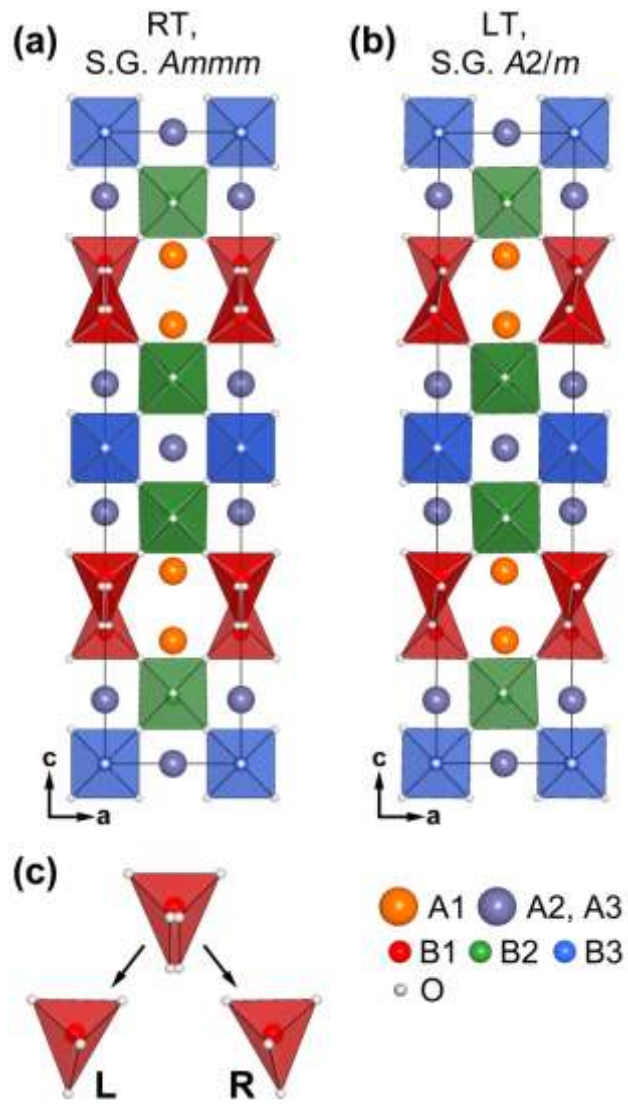
Figure 8. Crystal structure of RT (a) and LT (b) $Pb_{2.4}Ba_{2.6}Fe_2Sc_2TiO_{13}$ and the scheme of disordered (*Ammm* space group) and ordered (*A*2/*m* space group) tetragonal pyramids in the CS block (c).

Tables

Table 1. Crystallographic parameters of $Pb_{2.4}Ba_{2.6}Fe_2Sc_2Ti_1O_{13}$ at T = 300 K and 2 K.

Composition	$Pb_{2.4}Ba_{2.6}Fe_2Sc_2Ti_1O_{13}$	
Temperature	300 K	2 K
Space group	*Ammm*	*A2/m*
a, Å	5.8328(1)	5.81765(9)
b, Å	4.07080(6)	4.05846(5)
c, Å	27.1395(5)	27.0944(5)
β, °	---	90.257(3)
Cell volume, $Å^3$	644.40(2)	639.71(2)
Z	2	2
Calculated density, g/cm^3	6.759	6.808
Radiation, wavelength	neutron, 1.4940Å	neutron, 1.8856Å
R_F, R_P, R_{wP}, %	0.016, 0.026, 0.032	0.011, 0.024, 0.030

Table 2. Positional parameters and ADPs for $Pb_{2.4}Ba_{2.6}Fe_2Sc_2TiO_{13}$ (T = 300 K).

Atom	Position	Occupancy	*x/a*	*y/b*	*z/c*	$U_{iso}(Å^2)$
A1	4*i*	1Pb	1/2	1/2	0.3051(1)	0.0141(7)
A2	4*i*	2/15Pb + 13/15Ba	0	0	0.1016(2)	0.021(1)
A3	2*d*	2/15Pb + 13/15Ba	1/2	1/2	1/2	0.015(2)
B1	4*i*	0.92Fe + 0.08Ti	0	0	0.2928(1)	0.0085(7)
B2	4*j*	0.71Sc + 0.23Ti + 0.06Fe	1/2	0	0.3949(1)	0.0087(8)
B3	2*b*	0.58Sc + 0.38Ti + 0.04Fe	0	0	1/2	0.003(1)
O1	8*n*	1	1/2	1/2	0.3881(2)	0.013(1)
O2	8*n*	1	0.249(1)	0	0.4455(2)	0.0107(5)
O3	8*n*	1	0.2597(6)	0	0.3337(1)	0.0144(7)
O4	8*n*	0.5	0.024(1)	0	0.2192(2)	0.011(1)
O5	2a	1	0	1/2	1/2	0.016(2)

Table 3. Positional parameters and ADPs for $Pb_{2.4}Ba_{2.6}Fe_2Sc_2TiO_{13}$ (T = 2 K).

Atom	Position	Occupancy	x/a	y/b	z/c	$U_{iso}(Å^2)$
A1	$4i$	1	0.5032(9)	1/2	0.3050(1)	0.0109(9)
A2	$4i$	2/15Pb + 13/15Ba	0.000(2)	0	0.1001(2)	0.012(1)
A3	$2d$	2/15Pb + 13/15Ba	1/2	1/2	1/2	0.009(2)
B1	$4i$	0.92Fe + 0.08Ti	-0.006(1)	0	0.2927(1)	0.0042(8)
B2	$4i$	0.71Sc + 0.23Ti + 0.06Fe	0.497(1)	0	0.3943(1)	0.006(1)
B3	$2b$	0.58Sc + 0.38Ti + 0.04Fe	0	0	1/2	0.008(2)
O1	$4i$	1	0.493(2)	1/2	0.3880(2)	0.009(2)
O2	$4i$	1	0.251(1)	0	0.4454(4)	0.006(1)
O2'	$4i$	1	0.247(2)	0	0.5554(3)	0.008(2)
O3	$4i$	1	0.243(1)	0	0.3349(3)	0.010(2)
O3'	$4i$	1	0.273(1)	0	0.6667(3)	0.006(2)
O4	$4i$	1	0.034(1)	0	0.2197(1)	0.008(1)
O5	$2a$	1	0	0	0	0.017(2)

Table 4. Selected interatomic distances (Å) for $Pb_{2.4}Ba_{2.6}Fe_2Sc_2TiO_{13}$ (T = 300 K).

A1-O1	2.251(6)	A3-O1	3.038(5) × 2	B2-O1	2.0438(5) × 2		
A1-O3	2.590(2) × 4	A3-O2	2.910(4) × 8	B2-O2	2.008(6) × 2		
A1-O4	2.851(7)	A3-O5	2.91639(9) × 2	B2-O3	2.173(4) × 2		
A2-O1	2.9297(7) × 2	B1-O3	1.878(4) × 2	B3-O2	2.073(5) × 4		
A2-O2	2.810(4) × 4	B1-O4	2.003(5)	B3-O5	2.03540(6) × 2		
A2-O3	3.085(4) × 4	B1-O4	2.066(1) × 2				
A2-O5	2.758(5)						

Table 5. Selected interatomic distances (Å) for $Pb_{2.4}Ba_{2.6}Fe_2Sc_2TiO_{13}$ (T = 2 K).

A1-O1	2.252(6)	A3-O1	3.034(5) × 2	B2-O1	2.0365(5) × 2
A1-O4	2.661(5) × 2	A3-O2	2.896(7) × 4	B2-O2	2.00(1)
A1-O5	2.529(4) × 2	A3-O3	2.925(7) × 4	B2-O2'	2.01(1)
A1-O6	2.778(8)	A3-O7	2.90882(9) × 2	B2-O3	2.180(8)
				B2-O3'	2.133(8)
A2-O1	2.89(1)	B1-O3	1.842(8)		
A2-O1	2.96(1)	B1-O3'	1.907(8)	B3-O2	2.082(9) × 2
A2-O2	2.786(8) × 2	B1-O4	1.991(5)	B3-O2'	2.08(1) × 2
A2-O3	2.769(8) × 2	B1-O4	2.063(1) × 2	B3-O5	2.02923(5) × 2
A2-O4	3.039(7) × 2				
A2-O5	3.140(7) × 2				
A2-O6	3.244(6)				
A2-O7	2.714(5)				

Supporting Information

Table S1. The ^{57}Fe Mossbauer hyperfine parameters of $Pb_{2.4}Ba_{2.6}Fe_2Sc_2TiO_{13}$: IS, isomer shift relative to α-Fe at ambient temperature; ΔE_Q, apparent quadrupole shift; H_{hf}, magnetic hyperfine field, <…> average value for distributions; Γ, line width; I, relative spectral area.

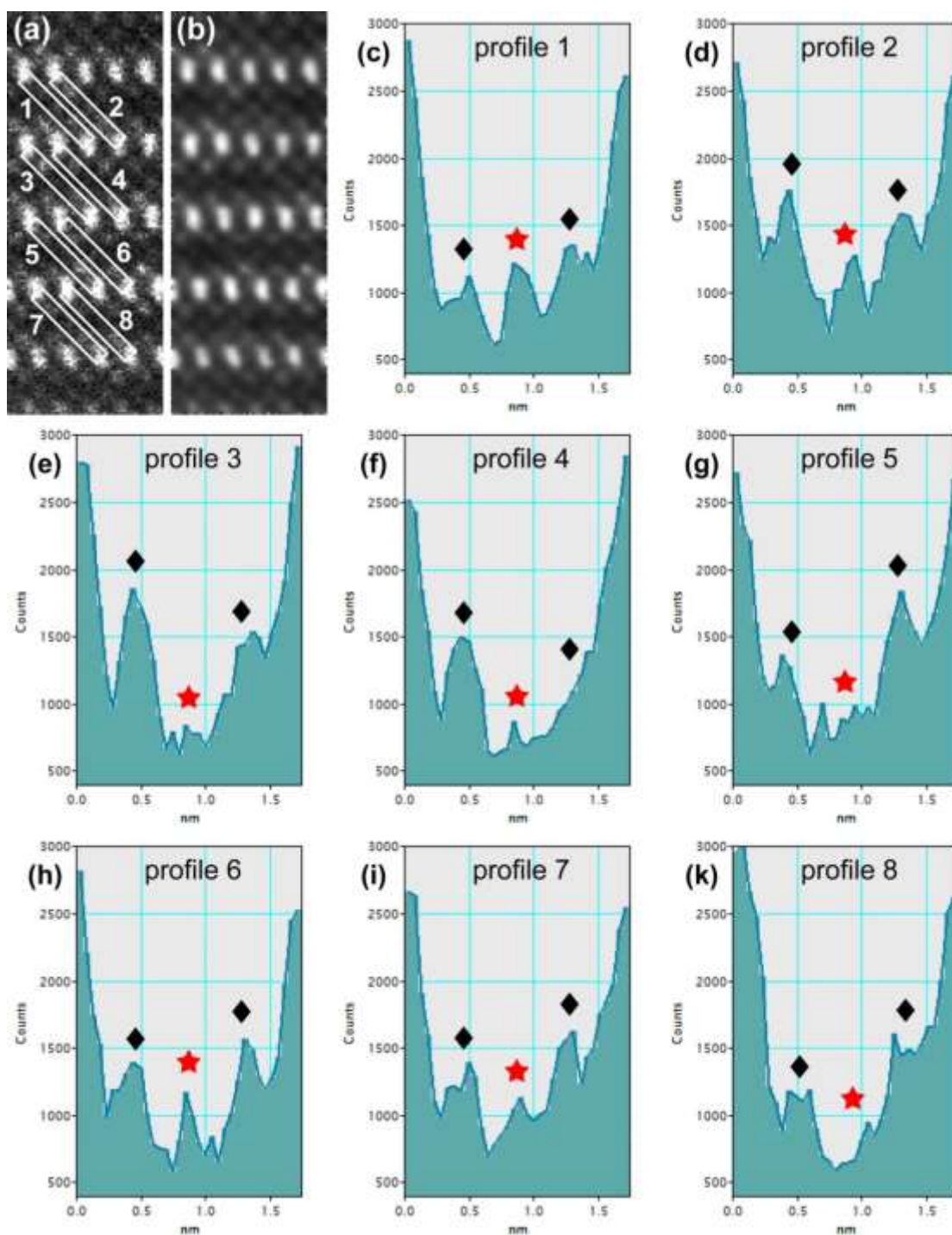| T, K	Comp.	IS, mm/s ± 0.01	ΔE_Q, mm/s ± 0.01	H_{hf}, T ± 0.2	I, % ± 1	Γ, mm/s ± 0.01
298	D1	0.31	0.84	-	61	0.35
	D2	0.33	0.56	-	32	0.31
	D3	0.36	0.52	-	7	0.32
78	D3	0.42	0.73	-	100	0.43
4.2	Di1	0.43	0.24	<44.9>	91	-
	S1	0.49	-0.07	49.4	9	0.52

Figure S1. (a) Experimental Fe STEM-EELS elemental map. (b) The same map after low-pass filtering. This operation significantly reduces the noise and hence improving visual interpretation of the image. (c-k) Intensity profiles measured on the experimental Fe-map along the [100] direction of the basic perovskite structure. The exact position, where the profiles were measured is indicated with the rectangles in figure (a). On the profiles, black diamonds indicate the B2 position, and red stars – the B3 positions. According to the profiles, the Fe occupancy in the B2 positions on average is significantly higher than in the B3 positions.
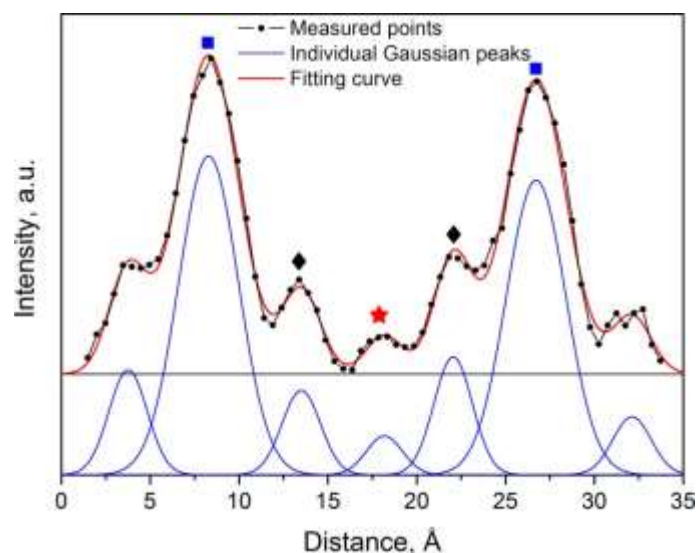
Figure S2. An averaged intensity profile of the Fe STEM-EELS elemental map (Figure S1a). For averaging, 12 individual [100] profiles were measured (similar to those in Figure S1), aligned with respect to the position of the peaks and summed up. B1-positions are indicated with the blue squares, the B2 – with black diamonds, the B3 – with a red star. The measured data were fitted with a set of Gaussian functions above a constant background. Because of the specific interaction of the electron beam with the crystalline matter, the intensity of the peaks can be treated qualitatively only. They confirm that the majority of Fe occupies tetragonal pyramids (the B1-sites) and minor fraction of Fe is present in both octahedral positions with prevalence in B2 rather than B3.
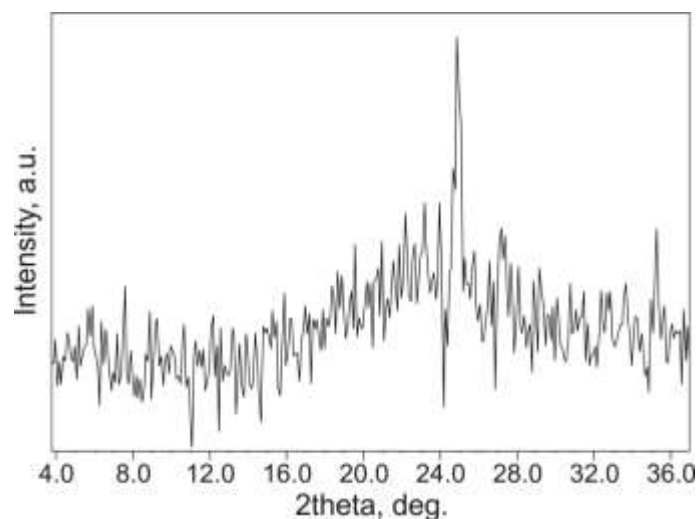

Figure S3. Difference curve between the RT and LT NPD data (λ = 1.8857 Å). One can notice the presence of weak diffuse intensity centered near 2θ = 23º. The sharp spike is a residual after the subtraction of the (006) nuclear reflection (2θ = 24.10º).

TOC image